

Impedance MPC with Disturbance Estimation for Dexterous Hand Control

Yongyan Cao

Abstract—Dexterous hands must simultaneously track precise finger trajectories and maintain safe, compliant contact—objectives in tension for any fixed-gain controller. We present an actuator-agnostic Impedance Model Predictive Control (Impedance MPC) framework for dexterous fingers, instantiating the constant- A_d offset-free architecture established for physical human–robot interaction (pHRI); its stability, recursive-feasibility, and input-to-state-stability guarantees are inherited by preserving the architectural assumptions. An algebraic feedforward reduces the tendon transmission—hydraulic, cable, pneumatic, twisted-string, or series-elastic—to a constant-coefficient double integrator, so the QP cost inverse is precomputed offline and a 10-step receding-horizon quadratic program runs at 500 Hz while enforcing hard constraints on contact force (ISO/TS 15066), actuation limits, and jerk. An encoder-only augmented-Kalman disturbance state drives steady-state error to zero under any constant contact load. On a hydraulically actuated finger—the worked example platform, adding pressure and cavitation constraints—the 500 Hz Kalman MPC attains 0.5 mrad RMS, 0.1 mrad steady-state, and 6.6 mrad peak deflection under 1.5 Nm contact: 183 \times , 1500 \times , and 23 \times better than classical impedance. The realized first-move stiffness (18 \rightarrow 323 Nm/rad with update rate) is independently verified. The architecture scales to a 16-DOF LEAP Hand MuJoCo simulation, recovering from 2.5 N grasp-load disturbances within 0.7 s.

Index Terms—Dexterous manipulation, impedance control, model predictive control, Kalman filter, disturbance rejection, tendon-driven hands, hydraulic actuation, LEAP Hand.

I. INTRODUCTION

DEXTEROUS robotic hands route actuation to the phalanges through tendon transmissions—hydraulic, cable, pneumatic, twisted-string, or series-elastic—each of which introduces reflected inertia, transmission damping, and platform-specific nonlinearities that complicate high-bandwidth finger control. At the same time, safe operation with grasped objects and human co-workers demands predictable, bounded contact forces, motivating the ISO/TS 15066 limit of 140 N at robot–human contact points [2]. Throughout this paper a hydraulically actuated finger serves as the worked example platform: hydraulics offers the highest force density but is also the most demanding transmission to control, introducing coupled pressure dynamics, configuration-dependent effective inertia, and compressibility resonance [1]. The framework itself is actuator-agnostic; Section III gives the substitutions for the other tendon architectures.

Classical impedance control [3] resolves the accuracy–safety trade-off by shaping the mechanical port behavior at

the joint, but stiffness and disturbance rejection cannot be optimized simultaneously: for $K_d = 10$ Nm/rad and $\tau_{\text{ext}} = 1.5$ Nm the steady-state error is $e_\infty = \tau_{\text{ext}}/K_d = 150$ mrad, independent of loop bandwidth, while integral action (PI impedance) introduces windup across sequential contact events [27], [28]. Admittance control [4], [5] instead yields toward contact—correct for rehabilitation and pHRI, but wrong for autonomous grasping, where contact is a disturbance to be rejected. MPC can resolve both objectives—predictive constraint enforcement plus offset-free disturbance rejection through an augmented estimator state [6]—but existing impedance MPC formulations either optimize impedance *parameters* as decision variables, limiting update rates to 10–30 Hz [7], [8], or compensate the estimated disturbance only reactively at the current step [9]. Neither achieves the sub-15 mrad precision window required for dexterous finger positioning under contact.

This paper takes as its base the constant- A_d offset-free Impedance MPC framework established for redundant-manipulator pHRI [29]—a two-layer design (feedforward reduction to a configuration-independent double integrator, plus a receding-horizon QP with an encoder-only Kalman disturbance state) whose stability, recursive feasibility, and input-to-state stability (ISS) are analyzed at the *architecture* level—and develops it for dexterous hands. Because the architecture operates on the residual error dynamics after feedforward reduction, it is independent of the actuation technology. The contributions of the present paper are the parts *not* contained in [29]:

- 1) **Platform reduction and substitution map** (Sections III–IV): an algebraic feedforward cancels the transmission’s reflected inertia and damping—derived in detail for the hydraulic example, with the substitutions for cable, pneumatic, twisted-string, and series-elastic tendons in Table I—reducing every platform to the constant- A_d double integrator of [29] and enabling 500 Hz operation with a precomputed QP cost inverse.
- 2) **Optional platform contact channel** (Section IV-B): the encoder-only offset-free Kalman estimator is inherited unchanged; where the hydraulic platform instruments slave-piston pressure P_2 for safety interlocks, a *sensorless* contact-torque estimate $\hat{\tau}_{\text{ext}} = A_2 P_2 J_f$ becomes available as an optional third measurement that shortens the contact-onset transient. It is not required for the offset-free guarantee and is not used in the reported results.
- 3) **Platform constraint embedding with recursive feasibility** (Section V): the actuation platform’s physical

Preprint, June 2026. This work has been submitted for possible publication; copyright may be transferred without notice.

Corresponding author: Yongyan Cao (e-mail: yongyancao@gmail.com).

limits enter the QP as constraints rather than post-hoc saturation—on the hydraulic example, cavitation, seal pressure, and the ISO/TS 15066 contact-force limit—with a soft-constraint relaxation that keeps the QP feasible under rigid impact.

- 4) **Benchmarks with independently verified realized impedance** (Sections VI–VII): seven-controller studies on sinusoidal tracking and precision reach-and-hold identify the 500 Hz update rate as the minimum requirement, for this plant and tuning, to suppress both contact-onset and release transients below a 15 mrad criterion; the realized first-move stiffness driving the no-Kalman results is verified by three independent routes (Section VI-C).
- 5) **16-DOF extension with a diagnosis and fix for the full-hand Kalman** (Section VIII): per-joint Impedance MPC scales to a LEAP Hand MuJoCo simulation; the three reasons the naïve per-joint Kalman fails on the coupled, contacting thumb—inertia mismatch, off-diagonal coupling, grasp self-contact—are isolated and removed in turn by gain scheduling, a coupled block estimator, and contact-aware conditional integration (thumb deviation $2329 \rightarrow 650 \rightarrow 236 \rightarrow 133$ mrad, the last *below* the 203 mrad no-Kalman baseline).

Section II surveys related work; Section III presents the tendon dynamics; Section IV the controller and the inheritance of its guarantees; Section V the platform constraints; Sections VI–VIII the simulation studies; Section IX concludes.

II. RELATED WORK

Impedance MPC. Cao *et al.* [7] optimize impedance parameters $\{M_d, D_d\}$ over a receding horizon with energy-tank passivity; because the parameters enter the prediction model nonlinearly, an iterative solver limits updates to 10–30 Hz. Here the decision variables are corrective *torques* and the constant A_d permits offline H^{-1} precomputation—a $15\text{--}50\times$ update-rate advantage—while the energy-tank constraint of Section V is directly inspired by [7]. Haninger *et al.* [8] jointly optimize force reference and impedance with Gaussian-process task models and probabilistic chance constraints; the present work instead uses a two-parameter analytic plant model, a hard deterministic ISO/TS 15066 bound, and an integrating disturbance state that achieves exactly zero steady-state error. Roveda *et al.* [10] adapt impedance parameters by model-based reinforcement learning, without per-step hard contact constraints or an offset-free estimator. Wu *et al.* [9] combine a linear MPIC with ADRC at 500 Hz, but the ESO compensates the disturbance only at the current step; here the estimate is propagated through all N prediction steps, which is why the controller pre-loads corrective torque and suppresses the contact-release transient to 6.6 mrad where reactive compensation retains 150 mrad peaks.

Dexterous hands. The LEAP Hand [11] trades accuracy for safety with intentionally compliant joints ($K_p = 3$ Nm/rad)—precisely the trade-off Impedance MPC removes by enforcing contact force as a constraint independent of tracking stiffness; its MuJoCo model is the baseline throughout. RL-based in-hand manipulation [12] achieves impressive policies without

formal guarantees on contact force or steady-state error, and safe contact reaction remains an open challenge [16]. Hogan’s impedance formulation [3], the force-control survey [18], and Merritt’s hydraulic text [1] underpin the models of Section III.

III. TENDON DYNAMICS

The controller of Section IV requires from the transmission only two scalar parameters—the effective joint inertia I_f^{eff} and damping b_f^{eff} —which exist for every tendon architecture. This section derives them for the hydraulic example platform and summarizes the substitutions for the alternatives (Table I).

A. Hydraulic Tendon (Example Platform)

1) *Lumped Model and Joint-Space Reduction:* The motor–piston–fluid–finger transmission is modeled as a lumped second-order plant in the incompressible limit [1]:

$$M_e \ddot{x}_2 + B_e \dot{x}_2 = \frac{A_2}{A_1} F - F_{\text{ext}} \quad (1)$$

where x_2 is the slave-piston displacement, $M_e = M_2 + M_1(A_2/A_1)^2$ and $B_e = b_2 + b_1(A_2/A_1)^2$ are the effective piston inertia and damping (master quantities reflected to the slave), F is the motor drive force (control input), F_{ext} the external contact force at the slave piston, and A_1, A_2 the piston areas. The finger linkage maps piston to joint motion through a scalar mechanism Jacobian $J_f(\theta_f)$ ($\dot{x}_2 = J_f \dot{\theta}_f$; $J_f = r_f$ constant for a linear tendon). Substituting and applying the virtual-work identity $\tau = J_f F$ yields the joint-space equation of motion

$$I_f^{\text{eff}} \ddot{\theta}_f + b_f^{\text{eff}} \dot{\theta}_f = \frac{A_2}{A_1} F J_f - \tau_{\text{ext}} \quad (2)$$

with $I_f^{\text{eff}} = M_e J_f^2$, $b_f^{\text{eff}} = B_e J_f^2$, and $\tau_{\text{ext}} = F_{\text{ext}} J_f$; the centripetal-like term $M_e J_f \dot{J}_f \dot{\theta}_f^2$ vanishes for a linear tendon and is absorbed into the lumped disturbance otherwise. The effective compliance $\Gamma_e = 1/I_f^{\text{eff}}$ plays the role of the operational-space inertia inverse $\Lambda^{-1}(q)$ in the Cartesian formulation of [29].

2) *Sensorless Contact-Torque Estimation:* No dedicated force sensor is assumed. The slave pressure P_2 provides a contact-force estimate from Newton’s law at the slave piston:

$$\hat{F}_{\text{ext}} = A_2 P_2 - M_2 \ddot{x}_2 - b_2 \dot{x}_2 \approx A_2 P_2 \quad (\text{quasi-static}) \quad (3)$$

and $\hat{\tau}_{\text{ext}} = \hat{F}_{\text{ext}} J_f(\theta_f)$ in joint space. Pascal’s law ($P_1 A_1 = P_2 A_2$ at quasi-static steady state) provides a redundancy check.

3) *Hydraulic Resonance and Bandwidth:* With finite bulk modulus β , the fluid column resonates at

$$\omega_h = \sqrt{\frac{\beta}{V_e} \left(\frac{A_1^2}{M_1} + \frac{A_2^2}{M_2} \right)} \quad (4)$$

≈ 3900 rad/s (≈ 620 Hz) at typical values ($\beta = 1.5 \times 10^9$ Pa, $A = 100$ mm², $V_e = 10$ mL, $M = 0.1$ kg)—well above the closed-loop bandwidth realized at the 100–500 Hz QP rates targeted here (dominant pole ≈ 615 rad/s at 500 Hz, Section VI-C).

Modeling limitations. The lumped plant (1) omits the servo-valve square-root flow nonlinearity, the temperature dependence of viscosity and bulk modulus, and finite-bandwidth compressibility. The first two are slowly varying and absorbed by the disturbance state \hat{d} ; the third is benign while $\omega_h \gg$ bandwidth, but stiff, fast rigid impacts that excite the compressibility mode fall outside the quasi-static pressure map of Section V-A and require an augmented-pressure-state model, left to future work. The present results are the rigid-fluid, in-bandwidth limit.

B. Other Tendon Architectures

Only the feedforward inversion, the values of $(I_f^{\text{eff}}, b_f^{\text{eff}})$, and the optional contact-measurement channel change across platforms; the error dynamics (6)–(7), estimator (8)–(9), and QP are untouched. *Cable tendons* [22]—the most common architecture (Allegro, LEAP [11], Shadow)—give $I_f^{\text{eff}} = I_m r_f^2 / r_m^2$ from motor and capstan geometry, with motor current or cable tension as the contact channel. *Pneumatic McKibben muscles* [23] require inverting the nonlinear force–pressure–length map in the feedforward and are bandwidth-limited to 5–10 Hz by air compressibility. *Twisted-string actuators* [24] require the nonlinear twist kinematics in the feedforward and suffer preload-dependent stiffness and wear. *Series-elastic actuators* [25] provide the cleanest contact channel—spring deflection measures transmitted torque directly—at the lowest bandwidth. Table I summarizes.

IV. IMPEDANCE MPC DESIGN

The two-layer architecture, force-form disturbance representation, offset-free Kalman estimator, and condensed-QP machinery are those of [29] and are only summarized here to fix notation; the reader is referred to [29] for derivations. New in this section are the hydraulic feedforward (5), the optional pressure measurement channel, the first-move characterization of the realized impedance (Section IV-D), and the explicit assumption-preservation argument under which the closed-loop guarantees of [29] transfer (Section IV-E).

A. Architecture and Error Dynamics

Layer 1 — Feedforward. An algebraic term cancels the known transmission dynamics, leaving a scalar double integrator as the residual plant:

$$F_{\text{ff}} = \frac{A_1}{A_2 J_f} \left[I_f^{\text{eff}} \ddot{\theta}_d + b_f^{\text{eff}} \dot{\theta}_f \right] \quad (5)$$

The inertia term uses the reference acceleration $\ddot{\theta}_d$; the damping term uses the *actual* velocity $\dot{\theta}_f$ so the physical damping cancels exactly. Only the two parameters $(I_f^{\text{eff}}, b_f^{\text{eff}})$, identified from a step response, are required.

Layer 2 — Impedance MPC. With $e = \theta_d - \theta_f$ and $F = F_{\text{ff}} + F_{\text{mpc}}$, the residual error dynamics are

$$\ddot{e} = -\Gamma_e(\theta_f) F_{\text{mpc}} + d(t) \quad (6)$$

where $d(t) = \tau_{\text{ext}} / I_f^{\text{eff}}$ lumps contact torque and unmodeled terms. The state $x_e = [e, \dot{e}]^\top$ obeys $\dot{x}_e = A_c x_e + B_c F_{\text{mpc}} +$

$E_c d$ with A_c the nilpotent double integrator, $B_c = [0; -\Gamma_e]$, $E_c = [0; 1]$. As in [29], the estimator and QP operate on the equivalent *force-form* disturbance $d_F \equiv -I_f^{\text{eff}} d (= -\tau_{\text{ext}}$ for a pure contact torque), which enters through the same input matrix as the control and is the quantity denoted \hat{d} below. Discretization is exact ($A_c^2 = 0$) and rate-independent in form:

$$A_d = \begin{bmatrix} 1 & \Delta t \\ 0 & 1 \end{bmatrix}, \quad B_d = \begin{bmatrix} -\frac{\Delta t^2}{2} \Gamma_e \\ -\Delta t \Gamma_e \end{bmatrix} \quad (7)$$

The constancy of A_d is the structural key inherited from [29]: the prediction matrices and the QP cost inverse H^{-1} are computed once offline, reducing each MPC step to a matrix–vector multiply (< 0.1 ms on embedded hardware). For configuration-varying mechanisms (slider-crank linkages; the thumb axle of Section VIII, whose inertia varies $26\times$), A_d remains exactly constant and only $B_d(\theta_f)$ —hence Γ , H^{-1} and the Kalman input blocks—is rescheduled online, an $O(N^2)$ update per step.

B. Offset-Free Disturbance Estimation

An integrating disturbance state is appended to the error state and estimated by a steady-state Kalman filter from **joint encoders alone** [29], [6], [20]:

$$\begin{bmatrix} x_e(k+1) \\ \hat{d}(k+1) \end{bmatrix} = \begin{bmatrix} A_d & B_d \\ 0 & 1 \end{bmatrix} \begin{bmatrix} x_e(k) \\ \hat{d}(k) \end{bmatrix} + \begin{bmatrix} B_d \\ 0 \end{bmatrix} F_{\text{mpc}}(k) + \begin{bmatrix} 0 \\ w_k \end{bmatrix} \quad (8)$$

$$y_k = \begin{bmatrix} 1 & 0 & 0 \\ 0 & 1 & 0 \end{bmatrix} [e, \dot{e}, \hat{d}]_k^\top + v_k \quad (9)$$

where the zero-mean white process noise w_k , of variance $Q_{\text{proc},d}$, drives *only* the disturbance state—the random-walk model $\hat{d}(k+1) = \hat{d}(k) + w_k$ (continuous time $\dot{d} = w$)—since the error states evolve deterministically once all unmodeled effects are lumped into d ; v_k is zero-mean white measurement noise with covariance R_{obs} . The random walk lets \hat{d} track constant and slowly varying contact loads. Zero steady-state error under constant disturbances requires detectability of the augmented pair [6], [21], which here reduces to the rank condition

$$\text{rank} \begin{bmatrix} I - A_d & -B_d \\ C_{x_e} & 0 \end{bmatrix} = n_x + n_d \quad (10)$$

satisfied whenever $\Gamma_e > 0$. The estimate converges in 5–10 QP periods; the convergence rate—hence the contact-onset peak—is set by the noise ratio $Q_{\text{proc},d}/R_{\text{obs}}$ (Section VI). Unlike PI impedance, the structured observer gain prevents wind-up across sequential contact events [27], [28]. A closed-loop analysis of the coupled observer–QP loop under *active* input saturation remains open, as in [29]; offset-free behaviour is established in the nominal (constraint-inactive, detectable) limit and verified numerically.

Remark 1 (Estimator-agnostic offset-free property). The offset-free property rests on the integrating internal model (8), not on the Kalman filter specifically: it holds for *any asymptotically unbiased estimator of the augmented state satisfying the detectability condition* (10) [6], [21]—e.g. a momentum observer or an ESO in the ADRC sense [9]. The

TABLE I
TENDON ARCHITECTURE COMPARISON

Architecture	Peak force density	Control bandwidth	Contact channel (replacing P_2)	Main limitation
Hydraulic (example platform)	High	50–500 Hz	Slave pressure P_2	Compressibility resonance; sealing
Cable tendon	Medium	100–1000 Hz	Motor current i_m or cable tension	Back-drivability; cable stretch
Pneumatic PAM	Medium	5–10 Hz	PAM gauge pressure	Low bandwidth; nonlinear map
Twisted-string	High	20–100 Hz	Motor current or string tension	Nonlinear kinematics; wear
Series-elastic	Low–Medium	10–30 Hz	Spring deflection δ	Low bandwidth; added compliance

estimator choice sets only the transient convergence rate and noise response.

Optional platform contact channel. Where slave pressure P_2 is instrumented (it typically already is, for safety interlocks), $y_3 = A_2 P_2 \approx -\hat{d}$ supplies a direct, low-latency third measurement of the same force-form disturbance, shortening estimator lag from 5–10 QP periods to ≈ 1 . It is optional—the offset-free guarantee holds from encoders alone—and is *not* exercised in the reported simulations; the term “sensorless” in Section III-A2 refers to the absence of a force/torque transducer. On other platforms the channel is replaced per Table I.

C. Receding-Horizon QP

Stacking N predicted states gives $Y = \Phi x_0 + \Gamma U + \bar{D} \hat{d}$, with Φ, Γ the standard prediction matrices built from (7) and $\bar{D}_k = \sum_{l=0}^{k-1} A_d^l B_d$ the cumulative disturbance propagator of [29] (the force-form \hat{d} enters through the same B_d as the control). Condensing the stage cost $\sum_k x_e^\top Q x_e + R_u F_{\text{mpc}}^2$ (terminal weight Q_f) yields

$$H = \Gamma^\top \bar{Q} \Gamma + R_u I_N, \quad f = \Gamma^\top \bar{Q} (\Phi x_0 + \bar{D} \hat{d}) \quad (11)$$

and the QP $\min_U \frac{1}{2} U^\top H U + f^\top U$ subject to

$$\begin{aligned} F_{\text{ff}}(k) + F_{\text{mpc}}(k) &\in [F_{\text{min}}, F_{\text{max}}] \quad (\text{motor bounds}) \\ \frac{A_2}{A_1} (F_{\text{ff}}(k) + F_{\text{mpc}}(k)) &\leq 140 \text{ N (ISO/TS 15066)} \\ |\Delta F_{\text{mpc}}(k)| &\leq \Delta F_{\text{max}} \quad (\text{jerk limit}) \\ P_{\text{vap}} \leq P_{2,k} &\leq P_{\text{max}} \quad (\text{cavitation/seal}) \end{aligned} \quad (12)$$

Only $F_{\text{mpc}}(0)$ is applied. The optional energy-tank passivity constraint of Section V-B, when enabled, adds one further row to (12). H^{-1} is precomputed; when no constraint is active the solve is the single multiply $U^* = -H^{-1}f$, and otherwise OSQP [13] or qpOASES [14] solves the small ($N=10$) QP warm-started in < 0.05 ms on a Raspberry Pi 4. The constant A_d is also what collapses the min–max LPV saturation formulation of [26] to a single nominal QP.

D. Equivalence to Classical Impedance and Realized Stiffness

In the unconstrained, disturbance-free, infinite-horizon limit with $Q = \text{diag}(K_d, D_d)$, $R_u \rightarrow 0$, the Impedance MPC recovers the classical impedance law $\tau^{\text{cmd}} = I_f^{\text{eff}} \ddot{\theta}_d + b_f^{\text{eff}} \dot{\theta}_d + K_d e + D_d \dot{e}$, giving the design rule $Q_{\text{pos}} = K_d$, $Q_{\text{vel}} = D_d$. At finite horizon and sampling rate the realized impedance differs from the target; we characterize it by the *first-move gain*

$$[k_e \ d_e] = -(H^{-1} \Gamma^\top \bar{Q} \Phi)_{1,:} \quad (13)$$

so that the applied input is $F_{\text{mpc}}(0) = k_e e + d_e \dot{e}$ when unconstrained. For the horizon, weights, and plant used in this paper, k_e increases with the QP update rate and saturates in Q_{pos} ; this monotonic rate dependence is a property of the specific tuning, established by direct computation and pole analysis in Section VI-C—not claimed as universal.

E. Stability, Recursive Feasibility, and ISS: Inheritance

No closed-loop guarantees are re-derived in this paper. The base framework [29] establishes, on the reduced system (6)–(8), (i) nominal asymptotic stability under the terminal Riccati cost with sufficient horizon, (ii) recursive feasibility via soft-constraint relaxation, and (iii) an ISS bound with respect to the estimation error $d - \hat{d}$. That analysis is embodiment-independent provided the following are preserved:

- A1 Bounded-error cancellation:** the feedforward (5) reduces the plant to (6) with residual mismatch absorbed into a bounded $d(t)$.
- A2 Stabilizable residual dynamics:** the double integrator (6) with $\Gamma_e > 0$, or its block-diagonal multi-finger extension.
- A3 Positive-definite cost:** $Q \succ 0$, $R_u > 0$, $Q_f \succeq Q$.
- A4 Convex constraints:** all rows of (12) linear in U , with the physical limits slack-relaxed (Section V-A) so the feasible set is never empty.

The hand embodiments satisfy A1–A4; in particular the hydraulic pressure limits enter as *quasi-static output constraints* on the same residual dynamics—pressure is *not* a prediction-model state—so the closed-loop system analyzed in [29] is structurally unchanged and the guarantees transfer directly; proofs are omitted. By Remark 1 the offset-free property likewise transfers under any detectable, asymptotically unbiased estimator. One boundary is explicit: in the compressibility regime of Section III-A3, P_2 must become a prediction state, the augmented model differs from the one analyzed in [29], and the inherited guarantees would require re-verification; that regime is excluded here.

V. PLATFORM CONSTRAINTS: THE HYDRAULIC EXAMPLE

The constraint-embedding pattern is platform-independent—any actuation technology contributes its physical limits as linear (or linearized quasi-static) inequalities on U , e.g. cable-tension positivity, PAM pressure bounds, SEA deflection limits. This section instantiates it on the hydraulic example.

A. Pressure Constraint and Recursive Feasibility

The seal limit $P_{2,k} \leq P_{\max}$ maps to a linear inequality on the command:

$$F_{\text{ff}}(k) + F_{\text{mpc}}(k) \leq \frac{A_1}{A_2} \left[A_2 P_{\max} - \frac{I_f^{\text{eff}}}{J_f} \hat{d}_k - B_e \dot{x}_{2,k} \right] \quad (14)$$

(the factor I_f^{eff}/J_f converts the Kalman estimate to piston-space force), and likewise for cavitation $P_{2,k} \geq P_{\text{vap}}$. Enforcing these inside the QP guarantees satisfaction at every predicted step—unlike post-hoc saturation, which alters the applied torque after the solve and violates passivity [17]. Two caveats: (i) the map is *quasi-static*— P_2 is treated as an algebraic output of the force balance, not as a state—justified by the timescale separation of Section III-A3: the fluid mode at $\omega_h \approx 3900$ rad/s settles within a fraction of each control interval, lying a factor ≈ 6 above the realized closed-loop bandwidth (dominant pole ≈ 615 rad/s at the 500 Hz rate, Section VI-C), so the pressure transient has decayed by the time the next QP samples it. When that separation fails, P_2 must be predicted as a state, with the consequence noted in Section IV-E. (ii) Hard physical limits can render the QP infeasible under rigid impact—if F_{ff} alone exceeds the pressure budget, no admissible F_{mpc} exists. The physical limits are therefore relaxed to penalized soft constraints,

$$\begin{aligned} \min_{U,s} \quad & \frac{1}{2} U^\top H U + f^\top U + \rho \sum_k s_k^2, \\ & \frac{A_2}{A_1} (F_{\text{ff}}(k) + F_{\text{mpc}}(k)) \leq F_{\text{contact,max}} + s_k, \quad s_k \geq 0 \end{aligned} \quad (15)$$

(and likewise for the pressure rows), keeping the torque/jerk box hard. This preserves the constant- A_d structure and guarantees recursive feasibility: the QP returns the *minimum-violation* command rather than faulting. A one-step check confirms the mechanism: under an impact feedforward that empties the hard set, the hard QP reports primal infeasible while the slacked QP returns the motor-saturated command with s equal to the unavoidable over-pressure. This is the same device used for the torque limit in [29] and is how assumption A4 is maintained.

B. Further Extensions

Passivity. An energy-tank constraint $T_{k+1} = T_k + \tau_{\text{ext},k} \dot{\theta}_{f,k} \Delta t - F_{\text{mpc},k} J_f \dot{\theta}_{f,k} \Delta t \geq 0$, linear in F_{mpc} , bounds the energy injected into the environment, extending [19], [7] to the receding-horizon setting. *Variable impedance.* Task-dependent compliance is obtained by scheduling $Q(t) = \text{diag}(K_d(t), D_d(t))$, e.g. lowering K_d when $\|\hat{\tau}_{\text{ext}}\|$ exceeds a contact threshold; the QP re-solves from the current state with no discontinuity. *Multi-finger.* Each finger runs an independent scalar QP; object-level grasp coordination adds a wrench condition coupling them into an nN -variable QP, solvable in < 1 ms for $n = 5$, $N = 10$.

VI. SIMULATION STUDY: DISTURBANCE REJECTION UNDER SINUSOIDAL TRAJECTORY

A. Scenario and Controllers

Seven controllers (Table II) track $\theta_d(t) = 0.8 + r(t)0.4 \sin(\frac{\pi}{2}t)$ rad ($r(t) = \min(1, t)$, smooth start) while a

TABLE II
CONTROLLERS EVALUATED IN SIMULATION

ID	Controller	Rate	Dist. est.	Paradigm
D1	Classical impedance ($K_d=10$)	1 kHz	None	Reactive
D2	Admittance ($K_a=3$)	1 kHz	None	Yield to contact
D3	PI impedance ($K_{\text{int}}=4$)	1 kHz	Integral	React. + integral
D4	Impedance MPC	100 Hz	None	Predictive
D5	Impedance MPC + Kalman	100 Hz	Kalman \hat{d}	Pred. + offset-free
D6	Impedance MPC	500 Hz	None	Predictive, fast
D7	Impedance MPC + Kalman	500 Hz	Kalman \hat{d}	Pred. + offset-free

TABLE III
SINUSOIDAL TRACKING RESULTS ($\tau_{\text{ext}} = 1.5$ NM, 16 s / 4 CYCLES)

Controller	RMS tot. (mrad)	RMS cont. (mrad)	Peak (mrad)	SS (mrad)
D1 — Impedance	91.7	149.1	150.6	150.1
D2 — Admittance	299.0	482.9	495.0	494.9
D3 — PI Impedance	72.3	98.8	147.3	74.4
D4 — MPC (no Kalman)	52.1	84.5	150.5	83.3
D5 — MPC + Kalman 100 Hz	10.3	15.3	150.6	0.1
D6 — MPC 500 Hz	3.1	5.1	6.4	4.7
D7 — MPC + Kalman 500 Hz	0.5	0.6	6.6	0.1

step contact torque $\tau_{\text{ext}} = 1.5$ Nm is applied from $t = 1.5$ to 3.0 s of each 4 s cycle and released; four cycles are simulated. Plant: $I_{\text{eff}} = 10^{-3}$ kg·m², $b_{\text{eff}} = 2 \times 10^{-3}$ Nm·s/rad, $\Gamma_e = 10^3$ rad²/Nm; the normalized disturbance $d = 1500$ rad/s² is large relative to the torque limit. All MPC variants use $N = 10$, $Q_{\text{pos}} = 10^8$, $Q_{\text{vel}} = 30$, $Q_{f,\text{scale}} = 5$, $R_u = 10^{-6}$, $\tau_{\text{max}} = 3$ Nm; D4/D5 run at 100 Hz, D6/D7 at 500 Hz, D5/D7 with the Kalman estimator.

The weight Q_{pos} is set near the sampling-rate stiffness ceiling: for this tuning the realized first-move stiffness (13) saturates at $k_e \approx 18$ Nm/rad at 100 Hz and reaches $k_e \approx 323$ Nm/rad at 500 Hz (verified in Section VI-C), both above the classical $K_d = 10$. Pushing Q_{pos} higher only saturates k_e (the 100 Hz ceiling is ≈ 20 , beyond which the discrete loop overshoots) while growing the Hessian conditioning (measured $\text{cond}(H) \approx 1.3 \times 10^6$ at 100 Hz, 1.1×10^5 at 500 Hz). The torque box is inactive in these tracking tasks, so the analytic H^{-1} solve is exact.

B. Results and Analysis

Table III reports RMS error over the full run, RMS and peak deflection within the force-on windows, and steady-state (SS) error at the end of each contact window; Fig. 1 shows the traces.

Baselines match theory. D1 reaches 150.1 mrad SS, matching $\tau_{\text{ext}}/K_d = 150$ mrad and validating the plant; D2 yields $\approx \tau_{\text{ext}}/K_a = 500$ mrad by design; D3's integral action converges too slowly within the 1.5 s contact window under its anti-windup limit (74.4 mrad).

No-Kalman MPC is stiffness-limited but already better than classical. With no disturbance state the QP is a predictive realization of an impedance with $e_\infty = \tau_{\text{ext}}/k_e$. At 100 Hz, $k_e \approx 18$ halves D1's error (83.3 mrad SS); at 500 Hz, $k_e \approx 323$ reaches 4.7 mrad SS—a 32× improvement with no estimator. Beyond the weight ceiling the *rate*, not the weight, is the

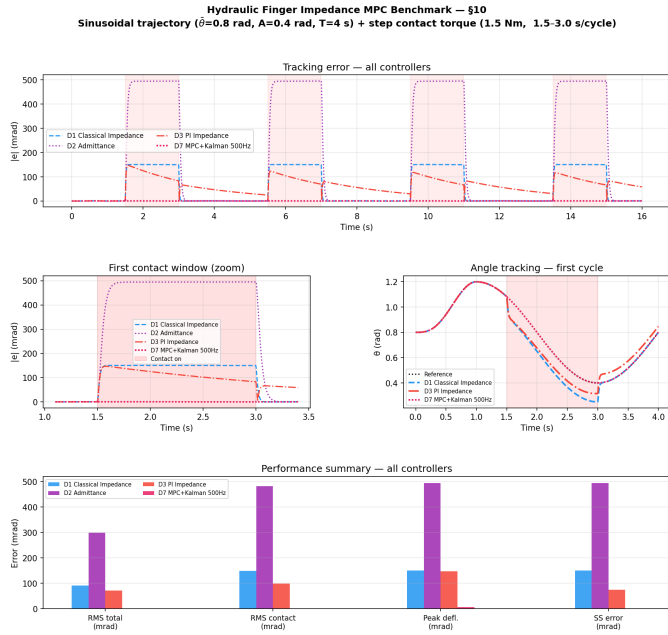


Fig. 1. Sinusoidal tracking under cyclic 1.5Nm step contact torque: the classical baselines (D1–D3) versus the proposed 500Hz Kalman MPC (D7). D7’s error (6.6mrad peak, 0.1 mrad steady-state) is barely distinguishable from zero at this scale; the remaining MPC variants are omitted for readability and reported in Table III.

lever. Two limits remain: a residual offset, and—at 100 Hz—a contact-onset peak (150.5 mrad) set by the 10 ms ZOH window that no weight choice removes (D6 peak: 6.4 mrad).

The Kalman estimator removes the offset; the rate governs the transient. Adding the estimator drives SS error to 0.1 mrad at both rates (833 \times at 100 Hz, 47 \times at 500 Hz): once \hat{d} converges, the disturbance is pre-canceled through all N prediction steps. Convergence takes 5–10 QP periods, so at 100 Hz the onset peak still builds to D1 levels (D5: 150.6 mrad) while at 500 Hz it is contained (D7: 6.6 mrad, 23 \times better than D1). The noise ratio $Q_{\text{proc},d}/R_{\text{obs}}$ sets the convergence speed. D7 is best on all four metrics; the rate and estimator contributions are orthogonal (transient vs. steady state) and additive. For reference, the LEAP Hand’s compliant design ($K_p = 3 \text{ Nm/rad}$) would deflect 500 mrad under this load; D7 holds 0.1 mrad while enforcing the ISO/TS 15066 limit as a hard constraint.

C. Independent Verification of the Realized Stiffness

The 18 \rightarrow 323 Nm/rad stiffness increase from a 5 \times rate change is the largest quantitative claim in the no-Kalman results, so it is verified by three independent routes that do not reuse the benchmark code path (script in the supplementary material). (1) *Gain extraction*: building H, Γ, Q, Φ directly from (7), (11) and evaluating (13) gives $k_e = 18.02$, $d_e = 0.190$ at 100 Hz and $k_e = 323.1$, $d_e = 0.823$ at 500 Hz. (2) *Closed-loop poles*: the eigenvalues of $A_d + B_d[k_e d_e]$ are $\{0, -0.802\}$ at 100 Hz and $\{0, -0.292\}$ at 500 Hz—Schur-stable, real spectra, the shrinking dominant pole confirming the faster loop tolerates the larger gain. (3) *Steady-state prediction*: $e_\infty = \tau_{\text{ext}}/k_e$ predicts 83.2 and 4.6 mrad; the

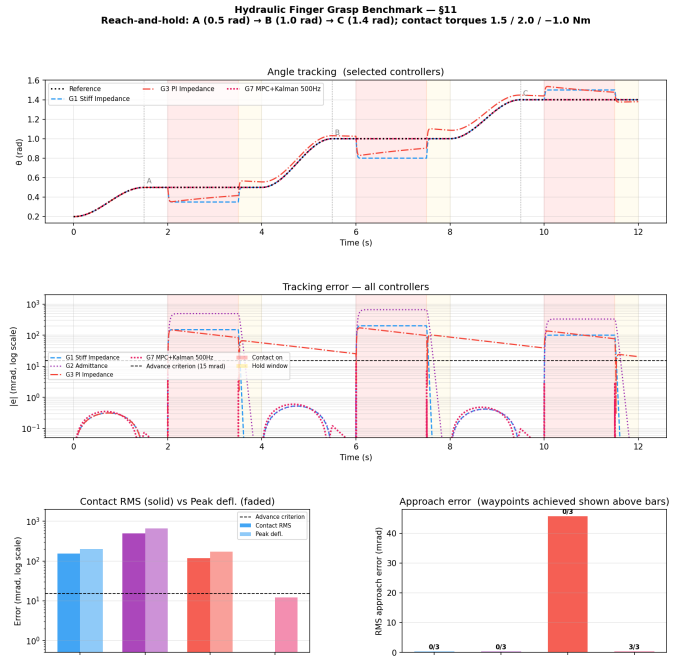


Fig. 2. Precision reach-and-hold benchmark: the classical baselines (G1–G3) violate the 15 mrad advance criterion at every waypoint, while the proposed G7 passes all three with zero steady-state error. The remaining MPC variants are omitted for readability and reported in Table IV.

closed-loop iteration reproduces these to three digits, and the full benchmark measures 83.3 (D4) and 4.7 mrad (D6)—agreement within 0.1 mrad. The mechanism is the sampled-data realization: with Q_{pos} saturated, the admissible first-move gain is bounded by the ZOH interval on this low-inertia plant, and shrinking Δt_{MPC} relaxes the bound. The claim established is that *for the chosen horizon, weights, and plant* the realized stiffness increases with update rate; no universal monotonicity across tunings is claimed.

VII. SIMULATION STUDY: PRECISION REACH-AND-HOLD UNDER OBJECT CONTACT

A. Scenario

Three sequential waypoints are commanded (A: 0.5 rad / 1.5 Nm; B: 1.0 rad / 2.0 Nm, both opposing flexion; C: 1.4 rad / 1.0 Nm into the joint stop), the contact firing 0.5 s after waypoint arrival. The *advance condition*—the precision requirement for dexterous grasping—is that the finger remain within 15 mrad of the waypoint for 0.5 s after the contact window closes.

B. Results and Analysis

Table IV and Fig. 2 report the results.

100 Hz fails on transients, not steady state. G1’s SS errors (τ_{ext}/K_d : 150/200/100 mrad) violate the criterion outright. G4 halves them ($k_e \approx 18$) yet is disqualified by a larger onset peak (295 vs. 200 mrad): over the 10 ms ZOH window the 2 Nm contact (2000 rad/s²) builds $\approx d\Delta t^2/2 = 100$ mrad of error before the QP responds, and the ZOH-held damping cannot arrest the momentum without overshoot—no (Q, R)

TABLE IV
PRECISION REACH-AND-HOLD RESULTS (ADVANCE CRITERION: $|e| \leq 15$ MRAD)

Controller	WP passed	RMS approach (mrad)	RMS contact (mrad)	Peak defl. (mrad)	SS @A/@B/@C (mrad)
G1 — Stiff Impedance	0/3	0.3	154	200	150 / 200 / 100
G2 — Admittance	0/3	0.3	501	660	495 / 660 / 330
G3 — PI Impedance	0/3	45.7	118	171	87 / 101 / 80
G4 — MPC 100 Hz	0/3	3.2	89	295	83 / 111 / 56
G5 — MPC + Kalman 100 Hz	0/3	0.3	25	300	0 / 0 / 0
G6 — MPC 500 Hz	3/3	0.3	5	12	5 / 6 / 3
G7 — MPC + Kalman 500 Hz	3/3	0.3	0.5	12	0 / 0 / 0

choice removes this; only the rate does. G5 reaches 0 mrad SS at every waypoint but fails on the *release transient*: at contact release \hat{d} still carries the previous load for 5–10 QP periods (50–100 ms at 100 Hz), overshooting to 300 mrad—a failure mode invisible in the cyclic averages of Section VI. G3 additionally shows 45.7 mrad approach error on the A→B ramp from integral wind-up accumulated at A—cross-contamination between contact events that the structured observer avoids.

500 Hz passes; the Kalman adds exactness. G6 keeps every deflection within the criterion (peak 12 mrad, SS 5/6/3 mrad) and passes 3/3 with no estimator; G7 converges within 2–4 updates at onset *and* release, holding the same 12 mrad peak with exactly zero SS error. For this plant and tuning, the 500 Hz rate is therefore necessary and sufficient to bring every contact transient within the precision window—at 100 Hz both MPC variants fail, each on a different transient.

VIII. 16-DOF EXTENSION: LEAP HAND MUJoCo SIMULATION

A. Setup and the Full-Hand Kalman

The single-finger controller extends to the 16-DOF LEAP Hand in MuJoCo [15] by running an independent per-joint scalar QP at 500 Hz, with per-joint I_{eff} and τ_{max} from mass-matrix measurements (Table V), feedforward damping cancellation per (5), and gravity compensation from the generalized bias force.

On the full hand the naïve per-joint Kalman fails on the thumb, for three separable reasons, each isolated and removed in turn:

(i) *Inertia mismatch → gain scheduling.* The thumb-axle inertia varies $26\times$ across the workspace; a fixed- I_{eff} Kalman reads the mismatch as a persistent disturbance and chases it. Because A_d never depends on I_{eff} , the inertia is gain-scheduled online from the mass-matrix diagonal, $I_{\text{eff}}(\theta) = M_{jj}(q)$, rebuilding only B_d, Γ, H^{-1} and the Kalman input blocks (Section IV-A). A scalar study sweeping the full $26\times$ range confirms: fixed-inertia RMS 1.2 mrad with 57 mrad/s jitter vs. gain-scheduled 0.4 mrad and 3 mrad/s—an $\sim 18\times$ reduction.

(ii) *Off-diagonal coupling → block estimator.* A per-joint (diagonal) estimator structurally cannot model the thumb’s off-diagonal mass coupling and chases the coupling torques: under a 2.5 N fingertip push at the power grasp, the per-joint Kalman reaches 2329 mrad thumb deviation (sometimes divergent) vs. 203 mrad with no Kalman; diagonal gain scheduling only partly helps (650 mrad). The fix is a *coupled block estimator* on the 4×4 thumb mass block $M_{\text{th}}(q)$: the residual is

TABLE V
PER-JOINT MPC PARAMETERS (LEAP HAND)

Joint type	I_{eff} (kg·m ²)	τ_{max} (Nm)	Rule
Finger MCP	4.74×10^{-4}	0.50	$I_{\text{min}} \times 3000 \text{ rad/s}^2$, capped
Finger ROT	5.46×10^{-5}	0.16	$I_{\text{min}} \times 3000 \text{ rad/s}^2$
Finger PIP	9.73×10^{-5}	0.29	$I_{\text{min}} \times 3000 \text{ rad/s}^2$
Finger DIP	1.47×10^{-5}	0.044	$I_{\text{const}} \times 3000 \text{ rad/s}^2$
Thumb CMC	4.80×10^{-4}	0.048	$I_{\text{avg}} \times 100 \text{ rad/s}$ (coupling)
Thumb AXL	9.90×10^{-6}	0.030	$I_{\text{min}} \times 3000 \text{ rad/s}^2$; hard cap
Thumb MCP	2.83×10^{-4}	0.028	$I_{\text{avg}} \times 100 \text{ rad/s}$ (coupling)
Thumb IPL	4.95×10^{-5}	0.005	$I_{\text{const}} \times 100 \text{ rad/s}$

the block double integrator $\ddot{e} = -M_{\text{th}}^{-1}(q)\tau_{\text{mpc}} + \dot{d}$ with a coupled $\hat{d} \in \mathbb{R}^4$. A 2-DOF study with strong coupling ($c/\sqrt{m_1 m_2} = 0.61$) isolates the mechanism: per-joint Kalman *worse* than none (738 vs. 127 mrad RMS), block Kalman best (38 mrad). On the full hand the block estimator removes the instability: 236 mrad deviation, no divergence.

(iii) *Self-contact → contact-aware integration.* At curled grasp poses the thumb’s self-contact forces are not in $M_{\text{th}}(q)$, so the integrating \hat{d} winds up against the unrejectable contact reaction. *Contact-aware conditional integration* suspends (leaks) the disturbance integration on joints registering a contact reaction and resumes the instant contact clears—the multi-DOF, contact-gated analogue of saturation anti-windup [27], [28]. With the gate, the thumb deviation falls to 133 mrad—*below* the 203 mrad no-Kalman baseline—and the gate is inert when the thumb is contact-free.

The progression 2329 → 650 → 236 → 133 mrad attributes the failure to inertia mismatch, coupling, and contact in turn, and reconciles the full hand with the unambiguously beneficial single-finger Kalman: a single finger has neither coupling nor self-contact. The full-hand results below use the conservative no-Kalman default; the block + contact-aware estimator is the validated upgrade. Remaining refinements (residual hold-jitter at contact, a contact-force-specific gate trigger) are noted in Section IX.

The thumb τ_{max} rules are deliberately tighter ($\times 100 \text{ rad/s}$ vs. $\times 3000 \text{ rad/s}^2$): aggressive CMC correction couples $\sim 3 \text{ Nm}$ onto the thumb MCP through the off-diagonal mass matrix, and the tighter bound ($\Delta v/\text{step} \leq 0.2 \text{ rad/s}$) prevents the resulting limit cycle. The thumb-axle cap $\tau_{\text{max}} = I_{\text{min}} \times 3000 = 0.030 \text{ Nm}$ retains a $26\times$ safety margin across its inertia variation pending the gain-scheduled estimate of Section VIII-A.

TABLE VI
16-DOF LEAP HAND RESULTS (PER-JOINT, ACROSS FOUR GRASPS)

Joint group	Track RMSE (mrad)	Settled offset (mrad)	Hold std (mrad)
Finger MCP ($\times 3$)	6–465	0–871	0–338
Finger ROT ($\times 3$)	0–13	0–29	0–11
Finger PIP ($\times 3$)	2–263	0–238	0–172
Finger DIP ($\times 3$)	0–133	0–341	0–88
Thumb CMC / MCP / IPL	9–164	4–209	0–142
Thumb AXL	12–79	1–80	0–72

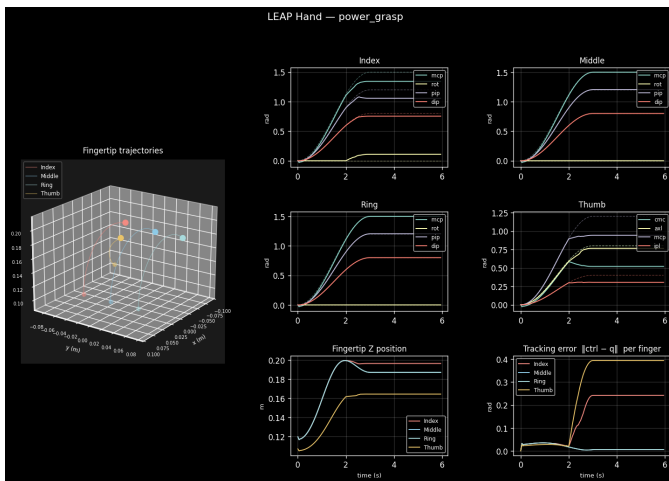


Fig. 3. Power-grasp dashboard for the 16-DOF LEAP Hand: per-joint tracking, contact equilibria, and rejection of the 2.5 N fingertip disturbance during the hold phase.

B. Results

Unlike the stiff single finger ($Q_{\text{pos}} = 10^8$), the 16-DOF hand runs soft impedance ($Q_{\text{pos}} = 2 \times 10^3$) with the conservative torque bounds of Table V for compliant grasping; per-joint tracking is intentionally loose, and during grasps the fingers settle to *contact equilibria*—the commanded closed pose is partly unreachable through the grasped object, a physically correct offset rather than a tracking failure. Four grasps (Open/Close, Precision Pinch, Power, Hook) with cosine-interpolated trajectories are evaluated; Table VI spans them (low end: gentle motions; high end: heavy-contact Power/Hook). A 25 mm, 50 g sphere is held stably in all four configurations.

The demonstrated multi-finger properties are stable grasping and disturbance rejection: a 2.5 N downward force—a slipping-load surrogate—is applied during the Power and Hook hold phases, to the middle phalanges at Power (so as not to reseat the fingertip–thumb contact) and to the fingertips at Hook. The push deflects the hand by 205 / 506 mrad (16-joint deviation norm, Power/Hook) and partially reseats the grasp: the contacting joints settle to a shifted contact equilibrium rather than returning to the pre-push pose. Measured against that post-release equilibrium, the transient decays below 15 mrad within 0.49 s (Power) and 0.71 s (Hook) (Fig. 3; quantitative thumb metrics in Section VIII-A). At the power-grasp pose the curled fingers contact the thumb; the resulting ~ 3 Nm constraint torques are not in the per-joint model, so

thumb joints settle 60–210 mrad from the geometric target at the contact equilibrium—physically correct—with bounded, non-divergent hold jitter that the contact-aware estimator of Section VIII-A suppresses.

IX. CONCLUSION

This paper developed the constant- A_d offset-free Impedance MPC architecture of [29] into an actuator-agnostic controller for dexterous fingers, with the hydraulic platform as the worked example: a two-parameter feedforward reduces any tendon transmission to the residual double integrator, platform limits enter the QP as soft-relaxed constraints, and the closed-loop guarantees transfer by preservation of the architectural assumptions (Section IV-E)—no new stability theory is claimed, and the compressibility regime where the inheritance would not apply is explicitly excluded.

The benchmarks established that (1) the no-Kalman MPC realizes a rate-dependent first-move stiffness (18 Nm/rad at 100 Hz, 323 Nm/rad at 500 Hz for this tuning—independently verified) that already beats classical impedance; (2) the encoder-only Kalman estimator removes the residual offset (0.1 mrad SS, $183\times$ RMS improvement); and (3) for this plant and tuning, 500 Hz is necessary and sufficient to keep both contact-onset and release transients within the 15 mrad precision window—the release transient being a 100 Hz failure mode invisible in cyclic metrics. The 16-DOF LEAP Hand extension showed the per-joint architecture scales without a full rigid-body model, and isolated the three reasons the per-joint Kalman fails on a coupled, contacting thumb, removing each (gain scheduling, block estimator, contact-aware integration) to land below the no-Kalman baseline.

Future work: maturing the contact-aware thumb estimator (a contact-force-specific gate trigger and a contact-consistent block model to remove the residual hold jitter); experimental validation on a hydraulic finger rig, including the servo-valve and compressibility effects excluded here, with re-verification of the inherited guarantees for the augmented-pressure-state model that regime requires; and integration with a learned grasp policy for impedance selection across object categories.

REFERENCES

- [1] H. E. Merritt, *Hydraulic Control Systems*. New York, NY: Wiley, 1967.
- [2] ISO/TS 15066:2016, *Robots and Robotic Devices—Collaborative Robots*. Geneva, Switzerland: International Organization for Standardization, 2016.
- [3] N. Hogan, “Impedance control: An approach to manipulation, Parts I–III,” *ASME J. Dyn. Syst. Meas. Control*, vol. 107, no. 1, pp. 1–24, Mar. 1985.
- [4] B. Siciliano and L. Villani, *Robot Force Control*. Norwell, MA: Kluwer Academic, 1999.
- [5] S. Haddadin, A. Albu-Schäffer, and G. Hirzinger, “Requirements for safe robots: Measurements, analysis and new insights,” *Int. J. Robot. Res.*, vol. 28, no. 11–12, pp. 1507–1527, 2009.
- [6] J. B. Rawlings, D. Q. Mayne, and M. Diehl, *Model Predictive Control: Theory, Computation, and Design*, 2nd ed. Madison, WI: Nob Hill Publishing, 2017.
- [7] Y. Cao, Z. Cheng, and C. Li, “Passive model-predictive impedance control for safe physical human–robot interaction,” *IEEE Trans. Cogn. Develop. Syst.*, vol. 16, no. 1, pp. 185–196, Feb. 2024.
- [8] K. Haninger, M. Hegeler, and L. Peternel, “Model predictive impedance control with Gaussian processes for human and environment interaction,” *Robot. Auton. Syst.*, vol. 168, p. 104493, Oct. 2023.

- [9] X. Wu, H. Huang, S. Cen, and B. Zhao, "Ensuring safe physical HRI: Integrated MPC and ADRC for interaction control," *Actuators*, vol. 14, no. 12, p. 608, 2025.
- [10] L. Roveda *et al.*, "Model-based reinforcement learning variable impedance control for human-robot collaboration," *J. Intell. Robot. Syst.*, vol. 100, no. 2, pp. 417–433, 2020.
- [11] K. Shaw, A. Agarwal, and D. Pathak, "LEAP Hand: Low-cost, efficient, and anthropomorphic hand for robot learning," in *Proc. Robot.: Sci. Syst. (RSS)*, Daegu, Republic of Korea, Jul. 2023.
- [12] M. Andrychowicz *et al.*, "Learning dexterous in-hand manipulation," *Int. J. Robot. Res.*, vol. 39, no. 1, pp. 3–20, Jan. 2020.
- [13] B. Stellato, G. Banjac, P. Goulart, A. Bemporad, and S. Boyd, "OSQP: An operator splitting solver for quadratic programs," *Math. Program. Comput.*, vol. 12, no. 4, pp. 637–672, 2020.
- [14] H. J. Ferreau, C. Kirches, A. Potschka, H. G. Bock, and M. Diehl, "qpOASES: A parametric active-set algorithm for quadratic programming," *Math. Program. Comput.*, vol. 6, no. 4, pp. 327–363, 2014.
- [15] E. Todorov, T. Erez, and Y. Tassa, "MuJoCo: A physics engine for model-based control," in *Proc. IEEE/RSJ Int. Conf. Intell. Robots Syst. (IROS)*, Vilamoura-Algarve, Portugal, Oct. 2012, pp. 5026–5033.
- [16] A. De Luca, A. Albu-Schäffer, S. Haddadin, and G. Hirzinger, "Collision detection and safe reaction with the DLR-III lightweight manipulator arm," in *Proc. IEEE/RSJ Int. Conf. Intell. Robots Syst. (IROS)*, Beijing, China, Oct. 2006, pp. 1623–1630.
- [17] M. Focchi, R. Featherstone, D. G. Caldwell, and C. Semini, "Torque-control based compliant actuation of a quadruped robot," in *Proc. 12th Int. Workshop Adv. Motion Control (AMC)*, Sarajevo, Bosnia and Herzegovina, Mar. 2012, pp. 1–6.
- [18] L. Villani and J. De Schutter, "Force control," in *Springer Handbook of Robotics*, B. Siciliano and O. Khatib, Eds. Berlin, Germany: Springer, 2016, ch. 7, pp. 195–220.
- [19] C. Ott, A. Albu-Schäffer, A. Kugi, and G. Hirzinger, "On the passivity-based impedance control of flexible joint robots," *IEEE Trans. Robot.*, vol. 24, no. 2, pp. 416–429, Apr. 2008.
- [20] R. E. Kalman, "A new approach to linear filtering and prediction problems," *ASME J. Basic Eng.*, vol. 82, no. 1, pp. 35–45, Mar. 1960.
- [21] G. Pannocchia and J. B. Rawlings, "Disturbance models for offset-free model-predictive control," *AIChE J.*, vol. 49, no. 2, pp. 426–437, Feb. 2003.
- [22] S. C. Jacobsen, E. K. Iversen, D. F. Knutti, R. T. Johnson, and K. B. Biggers, "Design of the Utah/MIT dextrous hand," in *Proc. IEEE Int. Conf. Robot. Autom. (ICRA)*, San Francisco, CA, Apr. 1986, pp. 1520–1532.
- [23] P. C. Chou and B. Hannaford, "Measurement and modeling of McKibben pneumatic artificial muscles," *IEEE Trans. Robot. Autom.*, vol. 12, no. 1, pp. 90–102, Feb. 1996.
- [24] I. Gaponov, D. Popov, and J. H. Ryu, "Twisted string actuation systems: A study of the mathematical model and a comparison of twisted strings," *IEEE/ASME Trans. Mechatronics*, vol. 19, no. 4, pp. 1331–1342, Aug. 2014.
- [25] G. A. Pratt and M. M. Williamson, "Series elastic actuators," in *Proc. IEEE/RSJ Int. Conf. Intell. Robots Syst. (IROS)*, Pittsburgh, PA, Aug. 1995, pp. 399–406.
- [26] Y.-Y. Cao and Z. Lin, "Min-max MPC algorithm for LPV systems subject to input saturation," *IEE Proc. Control Theory Appl.*, vol. 152, no. 3, pp. 266–272, May 2005.
- [27] Y.-Y. Cao, Z. Lin, and D. G. Ward, "Anti-windup design of output tracking systems subject to actuator saturation and constant disturbances," *Automatica*, vol. 40, no. 7, pp. 1221–1228, Jul. 2004.
- [28] Y.-Y. Cao, Z. Lin, and D. G. Ward, "An antiwindup approach to enlarging domain of attraction for linear systems subject to actuator saturation," *IEEE Trans. Autom. Control*, vol. 47, no. 1, pp. 140–145, Jan. 2002.
- [29] Y. Cao and J. Tang, "Impedance MPC for physical human-robot interaction: Predictive disturbance rejection with joint-limit safety," arXiv:2606.08281, Jun. 2026.